Journal of Colloid and Interface Science 714 (2026) 140182

Contents lists available at ScienceDirect

Journal of Colloid And Interface Science

journal homepage: www.elsevier.com/locate/jcis

Effects of interfacial rheology on shear-induced dynamics of MXene-covered droplets

Benedetta Attaianese [a], Gangamallaiah Velpula [b], Jennifer Theissen [c,d], Leonard M.C. Sagis [e], Ruth Cardinaels [a,f,*]

[a] Soft Matter Rheology and Technology, Department of Chemical Engineering, KU Leuven, Celestijnenlaan 200J, Leuven, 3001, Belgium
[b] Division of Molecular Imaging and Photonics, Department of Chemistry, KU Leuven, Celestijnenlaan 200F, Leuven, 3001, Belgium
[c] Centre for Membrane Separations, Adsorption, Catalysis, and Spectroscopy, Department of Microbial and Molecular Systems, KU Leuven, Celestijnenlaan 200F, Leuven, 3001, Belgium
[d] Institute for Materials Research (Imo-Imomec), Analytical and Circular Chemistry (ACC), NMR group, Hasselt University, Agoralaan Building D, Diepenbeek, 3590, Belgium
[e] Laboratory of Physics and Physical Chemistry of Foods, Wageningen University, Bornse Weilanden 9, Wageningen, 6708WG, The Netherlands
[f] Processing and Performance of Materials, Department of Mechanical Engineering, TU Eindhoven, P.O. Box 513, Eindhoven, 5600 MB, The Netherlands

ARTICLE INFO

Keywords:
Interfacial rheology
MXenes
Droplet dynamics
2D particles
Pickering emulsions

ABSTRACT

Hypothesis: Liquid-liquid interfaces covered by nanosheets such as MXenes represent versatile building blocks for multiphase materials in many applications. Due to their high hydrophilicity, MXene nanosheets assemble at the interface only when interacting with other stabilizers such as cationic surfactants. Depending on the surfactant properties, such as the number of charged head groups, the nanosheet-surfactant interactions result in distinct interfacial network structures and interfacial rheological properties, which influence the dynamics of MXene-covered droplets.

Experiments: This study uses interfacial shear and dilatational rheological techniques, such as double wall ring (DWR) rheometry and pendant drop tensiometry, to characterize the mechanical properties of the interfacial network formed by different MXene-surfactant complexes. The dynamics of single MXene-covered droplets are investigated by analyzing the deformation, breakup, and retraction behavior in a shear flow cell.

Findings: Our findings suggest that the rheological properties of nanosheet-covered interfaces can be tailored by using surfactants with a different number of charged head groups, thereby changing the interfacial network structure. The interfacial network, and more in particular the interfacial shear properties in the non-linear regime, influence the dynamics of droplets under shear flow, ranging from solid-like droplets with a brittle interfacial network to droplets with an elastic interface that show a residual deformation after cessation of shear.

1. Introduction

Particle-laden interfaces play a central role in biphasic systems such as Pickering emulsions. The particles used as stabilizers can be tailored to specific applications and are present in different morphologies ranging from simple spherical particles such as SiO_2 [1] or polymeric particles [2] to protein agglomerates [3], flexible microgels [4], 1D particles [5] and 2D particles [6]. When adsorbed at liquid-liquid interfaces, these particles form networks that enhance mechanical stability and enable applications in food technology, drug delivery, and functional multiphase materials [7,8]. Pickering emulsions stabilized by 2D particles, including conductive MXenes and graphene oxide (GO), are particularly attractive for designing composite materials, where interfacial networks provide elasticity and connectivity for structural fidelity and electrical percolation [9–12]. In this context, the response of the 2D particle-laden interfacial network to deformation is essential to understand the general processability of biphasic materials like Pickering emulsions and to optimize the mechanical and conductive properties of the final products.

Particles at interfaces introduce additional in-plane stresses under deformation, with both shear and dilatational elasticity contributions [13], therefore leading to shear and dilatational storage moduli (G_s' and E_s') higher than the loss moduli (G_s'' and E_s'') [14]. Prior work has shown that particle shape, concentration, and interaction forces strongly influence the interfacial network mechanics. Ellipsoidal par-

* Corresponding author.
E-mail addresses: benedetta.attaianese@kuleuven.be (B. Attaianese), gm.velpula@kuleuven.be (G. Velpula), jennifer.theissen@kuleuven.be (J. Theissen), leonard.sagis@wur.nl (L.M.C. Sagis), ruth.cardinaels@kuleuven.be (R. Cardinaels).

https://doi.org/10.1016/j.jcis.2026.140182
Received 21 August 2025; Received in revised form 2 February 2026; Accepted 22 February 2026
Available online 27 February 2026

ticles, for example, create stronger networks than spherical ones due to enhanced capillary interactions both from tip-tip and side-side particle interactions [15]. For 2D particles, multiple interaction modes can contribute to interfacial strength [16]. Depending on the surface coverage, the mechanical properties of the network can be driven by side-side particle interactions, but also particle-particle stacking can become significant for high surface coverage regimes. These features make 2D particle-laden interfaces promising candidates for applications requiring highly interconnected networks, such as conductive composites [17,18].

Despite their potential, the interfacial rheology of two-dimensional particles remains sparsely explored, particularly for multilayer assembly at liquid-liquid interfaces. Existing studies mainly focus on GO monolayers with low to high surface coverage created through controlled deposition and compression at water-air interfaces [17,19], but not the more complex, multilayered structures and liquid-liquid interfaces relevant for practical emulsion formulation. In applications such as Pickering emulsions for 3D printing, particle adsorption at the water-oil interface is not controlled, and the high particle concentrations commonly used make multilayer stacking highly likely. This aspect remains largely unexplored in the literature and is central to understanding the behavior of 2D particle-laden droplets under flow. Despite the growing interest in MXene-based Pickering emulsions [9,20–22], little is known about the mechanical properties of MXenes-laden interfaces. A first attempt to study self-assembled nanosheet-covered water-oil interfaces at high particle concentration was done by Kamkar et al. [23]. In their study, the interfacial rheological properties of GO nanosheets were investigated, demonstrating that GO interfacial stacking creates a solid-like network at the interface that can stabilize 3D-printed filaments in silicone oil [23]. However, the results primarily focus on linear interfacial rheology, whereas nonlinear rheology, which is essential for understanding interfacial behavior under realistic flow conditions such as in droplet dynamics, remains far less explored [24].

Furthermore, while interfacial viscoelasticity is often linked to bulk emulsion behavior [10,25], the connection between interfacial rheology and single-droplet dynamics under flow is still not well understood. Yet this droplet-level behavior is essential, as the deformation and recovery of particle-laden droplets directly affect processability, structural connectivity, and functional properties such as electrical percolation in MXene-based systems. For Newtonian droplets in Newtonian matrices, classical deformation models such as those of Taylor and Maffettone-Minale represent the interfacial stresses solely through a constant interfacial tension [26,27]. In particle-laden systems, however, the interface can strongly alter droplet deformation, induce breakup instabilities [28–30], and lead to irreversible deformation during retraction [31]. While Zhao et al. showed that dilatational elasticity can influence extensional droplet dynamics through an elasticity-based capillary number [32], shear and dilatational contributions generally act simultaneously, and their relative roles remain unclear. On the other hand, several theoretical studies have attempted to incorporate interfacial viscoelasticity [33–35], but these models rely on linear interfacial properties and typically treat shear and dilatation through effective viscosities or linear moduli. They do not account for the nonlinear, deformation-dependent interfacial mechanics that arise at high strains and may be relevant for droplet deformation.

This study investigates how $Ti_3C_2T_X$ MXenes modify the interfacial rheology of water-oil interfaces and how these interfacial properties translate into single droplet dynamics. Because $Ti_3C_2T_X$ nanosheets are highly hydrophilic and negatively charged, they remain dispersed in water and show limited spontaneous adsorption at the water-oil interface. To promote interfacial assembly, we introduced oppositely charged surfactants into the oil phase, forming MXene-surfactant complexes through electrostatic interactions. This particle-surfactant strategy is widely used to stabilize Pickering emulsions with particles of low intrinsic interfacial activity [36]. However, whereas prior work has focused primarily on structural stabilization [22,37–39], the interfacial rheological properties of platelet-laden oil-water interfaces and their role in governing flow-induced droplet deformation remain largely unexplored. Here, we use MXene-surfactant complexes specifically to probe how interfacial assembly controls both interfacial mechanics and droplet dynamics. To this end, we compare the interfacial networks formed by MXenes and surfactants with different numbers of charged head groups and use interfacial rheological characterization to establish how these distinct assemblies dictate the deformation and recovery dynamics of MXene-covered droplets under flow.

2. Materials and methods

2.1. Materials

Ti_3AlC_2 MAX phase with particle size $\leq 40\ \mu$m was purchased from Carbon Ukraine. Polydimethylsiloxane (PDMS5) with a viscosity of 5 mPas was purchased from SigmaAldrich and used as an oil phase for interfacial shear rheology and pendant drop tensiometry, while PDMS with a viscosity of 60 Pas (PDMS60 Rhodosil Bluestar) was selected for the droplet dynamics experiments. Monoaminopropyl-terminated polydimethylsiloxane (monoPDMSNH$_2$, Gelest, $M_W = 2000$ g/mol) and biaminopropyl-terminated polydimethylsiloxane (biPDMSNH$_2$, SigmaAldrich, $M_W = 2500$ g/mol) were used as cationic surfactants in the oil phase. MilliQ water (Sartorius Stedim Arium 611DI, 0.055 $\mu S/cm$) was used to prepare the aqueous phase.

2.2. Methods

2.2.1. Synthesis of $Ti_3C_2T_X$ MXene sheets

$Ti_3C_2T_X$ MXene sheets were synthesized using an adapted MILD method [40]. Ti_3AlC_2 MAX phase was etched by adding 1g of MAX powder to a solution of 9M LiF and 12M HCl. The etching solution was stirred at 500 rpm and room temperature for 24 h. Subsequently, the sample was washed by diluting with MilliQ water and centrifuging at 3500 rpm (BeckmanCoulter, Avanti J-30I, rotor JA-18) for 5 minutes for several cycles until pH≥5. The supernatant was then collected and further processed in an ultrasonic bath (Elmasoni S 30 H, 80W) for 1 h to promote the delamination of single-layer nanosheets and the formation of a stable colloidal suspension. Lastly, the sample was centrifuged for 1h to separate the stable single-layer particle suspension from the multi-layer $Ti_3C_2T_X$ and the unreacted MAX phase. The collected samples were characterized by performing SEM/EDX, XRD, AFM and DLS (see Section S1.1 for detailed information). From the SEM/EDX data of the MXenes clay (Table S1-S2), it is clear that the content of Al drops significantly compared to the initial percentage, indicating that the MAX phase has been successfully etched. The DLS data indicate an average hydrodynamic diameter of $205.3 \pm 2.2\ nm$. As previously demonstrated in the literature, this dimension gives a good estimation of the average lateral size of the platelets [41]. The XRD pattern in Fig. S3 shows the presence of the characteristic (002) peak of $Ti_3C_2T_X$ at 6.5° and the absence of the MAX phase peak at 9.5° in the supernatant, confirming the successful etching of Ti_3AlC_2. Fig. S4 shows the AFM images of MXenes flakes deposited on a mica substrate. The height of the flakes is around 2 nm, in agreement with the average height of single-layer MXenes [42].

2.2.2. Interfacial shear rheology

The interfacial shear rheological properties of water-PDMS5 interfaces were determined with a double wall-ring geometry (DWR) attached to a stress-controlled rheometer (DHR-3, TA Instruments). A Teflon cup with a stepwise edge and outer radius of 22 mm was directly placed onto a Peltier bottom plate and filled with a MXene aqueous suspension as bottom phase and a solution of PDMS5 and amino-terminated PDMS as top phase. Low viscous silicone oil (5 mPas) was chosen to reduce the effects of the bulk on the interfacial measurements.

Since the Boussinesq number $Bo_s \gg 1$ (Section S1.2), subphase drag is expected to be small compared to interfacial stresses and has been neglected [43].

The evolution of the interfacial network assembly was monitored by performing time sweep tests at 1 rad/s with a 0.01% strain for 4 hours. The viscoelastic properties of the interface were then assessed by performing frequency sweeps from 10^{-1} rad/s to 10^{1} rad/s at 0.01% strain to keep the sample in the linear region and an amplitude sweep from 0.001% to 100% strain at 1 rad/s. The limits of the nonlinear regime and, therefore, the critical strain γ_c and critical stress σ_c, were determined by calculating the strain at which G_s' deviates more than 5% from the initial plateau value. The strain and stress at the flow point, γ_f and σ_f, instead, were calculated as the strain at which $G_s' = G_s''$. To ensure reproducibility, the experiments were repeated 3 times for each particle concentration. For all tests, the temperature was kept constant at 21 °C. Creep tests were performed by applying a series of constant stresses for 90 minutes each and monitoring the sample recovery for another 90 minutes. The stress value was increased step-wise until a viscous behavior was observed in the sample. The tests were repeated twice, and both data sets gave similar results. Additionally, the recovery of the interfacial network was measured with thixotropy tests by following the evolution of the interfacial assembly at 1 rad/s with a 0.01 % strain for 4 hours, then shearing the interface at 1 1/s for 5 minutes and monitoring the viscoelastic recovery at 1 rad/s with a 0.01 % strain.

2.2.3. Pendant drop tensiometry

The interfacial tension was measured with a ThetaFlex (Biolin Scientific) device. For each experiment, a 20 μL droplet of water or MXene aqueous suspension was formed with a 18 gauge needle in a glass cuvette filled with PDMS5 and surfactant. The interfacial tension was monitored for 15 minutes by fitting the droplet shape to the Young-Laplace equation until reaching a steady state value. The response of the particle network to the dilatation of the interface was investigated by performing oscillating pendant drop experiments. Frequency sweeps at a strain of 1% from 0.01 Hz to 1 Hz were performed using a piezoelectric module (Pulsating drop module PD200). Large amplitude oscillatory measurements were, instead, performed on the Tracker™ Automatic Droplet Tensiometer with a step motor from Teclis. Also in this case, the droplet was stabilized for 15 minutes before proceeding with oscillatory experiments to investigate the dilatational viscoelasticity of the system. Amplitude sweeps were performed at 0.05 Hz from 3% to 50% strain. For all the experiments, the concentration of surfactants was kept fixed (2wt%) and above the critical micellar concentration (Fig. S6). Only conditions for which the droplets underwent homogeneous deformation are reported in the results section (see Section S1.3 for more details).

2.2.4. Droplet dynamics experiments

A TwinDrive rheometer (MCR 702, Anton Paar) in counter-rotating mode, combined with a stereo microscope, was used to perform in-situ visualizations of single droplet dynamics in shear flow (Fig. S8) [44]. Two glass parallel plates are inserted in a glass cup containing the PDMS60 matrix. Before each experiment, an aqueous droplet of $R_d = 250 \pm 10\mu$m is injected in the PDMS60 matrix from the top with a 26 gauge needle, the top plate is then slowly lowered to avoid bubble formation until the gap reaches 3 mm ($H/R_d = 12$). Subsequently, the droplet is left to rest for 30 minutes to allow the interfacial network to stabilize. The viscosity of the matrix has been chosen to avoid droplet sedimentation within the experimental time frame (Section S1.4). The radial distance of the droplet from the center of the plates is controlled to ensure that the edges of the plates do not influence the shear rate at the droplet location [45].

Shear-induced droplet dynamics are microscopically monitored from the velocity-vorticity plane (top view) and the velocity-velocity gradient plane (side view). The droplet deformation as a function of the capillary number is determined by applying a series of increasing constant shear rates while images are taken in both the front and top view. Each shear rate is applied until a steady state deformation is obtained. The capillary number is calculated by considering the interfacial tension measured with the pendant drop tensiometer. Additionally, the breakup behavior is investigated by step-wise increasing the applied shear rate until the droplet breaks. For each particle concentration, the experiments are repeated on 3 different droplets.

Table 1
Bulk concentrations c_b used for each experiment with the respective interfacial area A_i, bulk volume V_b and layer number l.

	A_i/V_b [cm^{-1}]	$l = 5$ c_b [mg/mL]	$l = 10$ c_b [mg/mL]	$l = 17$ c_b [mg/mL]
Counter-rotating	120	0.500	1.000	1.750
Pendant drop	17	0.071	0.141	0.248
DWR	1	0.004	0.008	0.014

The images are analyzed using a Matlab script to determine the droplet dimensions in the velocity-vorticity plane (projected length L_P and width W) and velocity-velocity gradient plane (length L, height B and orientation angle θ) (see Section S1.4 and Fig. S8).

2.2.5. In-situ visualization of the interfacial network

The structure of the interfacial network was visually investigated with confocal microscopy in reflection mode. A flat water-PDMS5 interface was created in a 7.5 × 7.5 mm^2 well. The central area of the well was visualized with a Leica TCS SP8 inverted confocal laser scanning microscope with a 20x/0.75 water objective. A solid-state laser with wavelength 488 nm was used to excite the interface, and the emission range of the detector was set between 475 and 505 nm.

2.2.6. Interfacial coverage calculation

Interfacial particle coverage plays a key role in the interfacial network properties. For each of the three techniques described in Sections 2.2.2–2.2.4, the interfacial area to bulk volume ratio is different. This means that using the same bulk concentration for all the experiments would lead to different surface coverages. Therefore, the samples have been formulated using fixed theoretical numbers of nanosheets at the interface $l = A_p/A_i$, where A_p is the surface area of the particles in the bulk phase and A_i is the actual interfacial area that is setup-dependent. A more standard approach to tune the surface coverage would involve controlled deposition, as often done for colloidal monolayers. However, due to the in situ electrostatic assembly of MXene platelets with the surfactant, direct deposition or controlled transfer of a known number of platelets onto the interface is not possible. The concentration of MXenes in the bulk phase was adjusted for each experiment to have a fixed amount of theoretical particle layers l using the formula $c_b = l\rho A_i/V_b$ (see Table 1). This calculation is based on the assumption that all the MXene nanosheets in the bulk go to the interface. Based on the average nanosheet lateral size ($\approx 200\ nm$), the nanosheet diffusion coefficient is $D = 1.1 \cdot 10^{-12}\ m^2/s$. In this condition, the average diffusion distance in a diffusion time of 30 minutes (i.e. waiting time of the counter-rotating experiment) is 90 μm, while the average droplet radius is 250 μm. This means that our assumption is probably a slight overestimation of the actual nanosheet surface coverage. However, preliminary deformation experiments were performed where droplets were deformed after different stabilization times to ensure that a steady state is reached after 30 minutes. Additionally, before each interfacial rheology experiment, time sweep measurements have been performed, as shown in Fig. S9 to ensure that the interfacial properties have reached steady state.

3. Results and discussion

3.1. Interfacial assembly

$Ti_3C_2T_X$ MXenes are strongly hydrophilic and form stable aqueous colloidal suspensions [42]. Therefore, they do not show interfacial activity when added to a biphasic system without any other stabilizer or

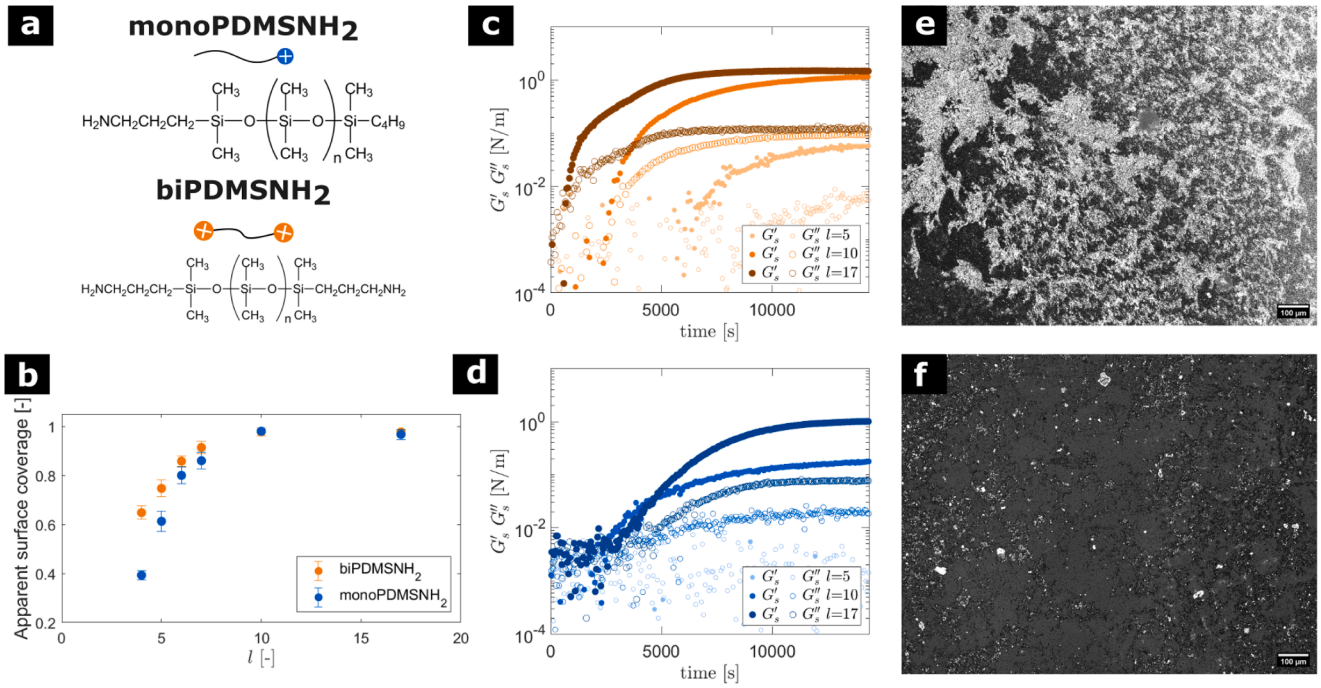

Fig. 1. (a) Schematic of monoPDMSNH$_2$ and biPDMSNH$_2$ and their chemical formulas. (b) Apparent surface coverage of water-PDMS5 interfaces stabilized by monoPDMSNH$_2$ and biPDMSNH$_2$. (c-d) Interfacial storage G_s' and loss G_s'' moduli for water-PDMS5 interfaces stabilized by MXenes and (c) biPDMSNH$_2$ or (d) monoPDMSNH$_2$, at a strain of 0.01%. (e-f) Confocal images of the interface stabilized by MXenes (l = 17) with (e) biPDMSNH$_2$ and (f) monoPDMSNH$_2$.

surface modification [20,21,46]. As Cain et al. used n-butylamine to interact with the MXene nanosheets electrostatically [22], we also exploited the electronegative charge of the MXenes to create nanosheet-surfactant complexes at the water-oil interface. Specifically, amino-terminated PDMS surfactants with either one or two terminal amine groups (monoPDMSNH$_2$ and biPDMSNH$_2$ in Fig. 1a) were dispersed in the oil phase. As the nanosheets and the amino-terminated PDMS are oppositely charged and dispersed in two different phases, they interact at the interface, forming an interfacial network. This strategy enables interfacial assembly without requiring chemical modification of the nanosheets, providing a more versatile route for incorporating MXenes at the interface.

This interfacial mechanism can be confirmed by comparing the interfacial properties of plain interfaces and interfaces covered with surfactant or nanosheet-surfactant complexes. The evolution of the interfacial network was monitored with pendant drop tensiometry and interfacial shear rheology. Fig. S9a and b illustrate the evolution of the interfacial tension over time with biPDMSNH$_2$ and monoPDMSNH$_2$, respectively. Droplets stabilized by MXene-PDMSNH$_2$ exhibit a lower interfacial tension than plain droplets and those stabilized only by surfactants. The steady state interfacial tension is not significantly influenced by the type of surfactant in the oil phase. Moreover, pendant-drop retraction experiments were used to estimate the apparent surface coverage of the two systems by identifying the onset of interfacial wrinkling (Section S2 and Fig. S10) [47]. The results in Fig. 1b reveal that MXene-monoPDMSNH$_2$ interfaces exhibit a lower surface coverage than MXene-biPDMSNH$_2$ ones, with both systems increasing in coverage until maximum packing is reached, for both, around $l \approx 10$.

The interfacial assembly dynamics were also examined on a flat interface using DWR rheometry. Figs. 1c-d show the time evolution of the interfacial storage (G_s') and loss (G_s'') moduli for the two types of nanosheet-surfactant complexes. In both cases, the moduli increase as nanosheets migrate from the aqueous phase and assemble into an interfacial network, reaching steady state only after more than two hours, which is substantially slower than the interfacial tension evolution kinetics (Fig. S9a-b). This slower response reflects the much larger diffusion length scale in the DWR geometry compared with the pendant-drop configuration.

For MXene-biPDMSNH$_2$ interfaces, low particle loads require more time to reach steady state. At l = 5, the steady-state G_s' is over an order of magnitude smaller than at $l \geq 10$, indicating that interfacial coverage increases with concentration until saturation. This trend is consistent with Popple et al. [48], who reported increasing MXene film thickness with bulk concentration in water-toluene systems, reaching a plateau only above ~ 5 mg/mL. At low loadings (l = 5, c_b = 0.004 mg/mL), the interfacial network remains below the jamming threshold and is governed by side-side nanosheet interactions rather than multilayer stacking. For $l \geq 10$, differences between concentrations diminish because interfacial coverage approaches saturation and additional stacking no longer significantly enhances viscoelasticity.

MXene-monoPDMSNH$_2$ interfaces behave differently. Their moduli are consistently lower than those of MXene-biPDMSNH$_2$ at the same loading. At l = 5, the response is inertia dominated, with a phase angle near 180°, indicating viscoelasticity below the instrument sensitivity, consistent with the much lower interfacial surface coverage at this concentration (Fig. 1b). Even at l = 17, the steady state value of G_s' continues to increase, but unlike the biPDMSNH$_2$ case, the particle concentration does not influence the time required to reach steady state.

The differences between the two MXene-PDMSNH$_2$ systems can be explained not only by their distinct surface coverage, which only differ significantly at low loading, but also by the different interaction mechanisms between nanosheets and surfactants, as previously suggested for particle-surfactant systems with spherical colloids [39,49]. Depending on the number of terminal -NH$_2$ groups, the complexes formed at the interface adopt different configurations: monoPDMSNH$_2$ can bind to a single nanosheet, whereas biPDMSNH$_2$ can bind to two sites on the same sheet or bridge between adjacent sheets. Such bridging effects have been reported to enhance network connectivity in emulsions stabilized by amino-terminated PDMS and spherical particles [49].

Direct imaging of these structures is challenging, as film-deposition approaches used in previous MXene and GO studies [19,48] may disturb the interfacial network and are not ideal for low-volatility oils such as

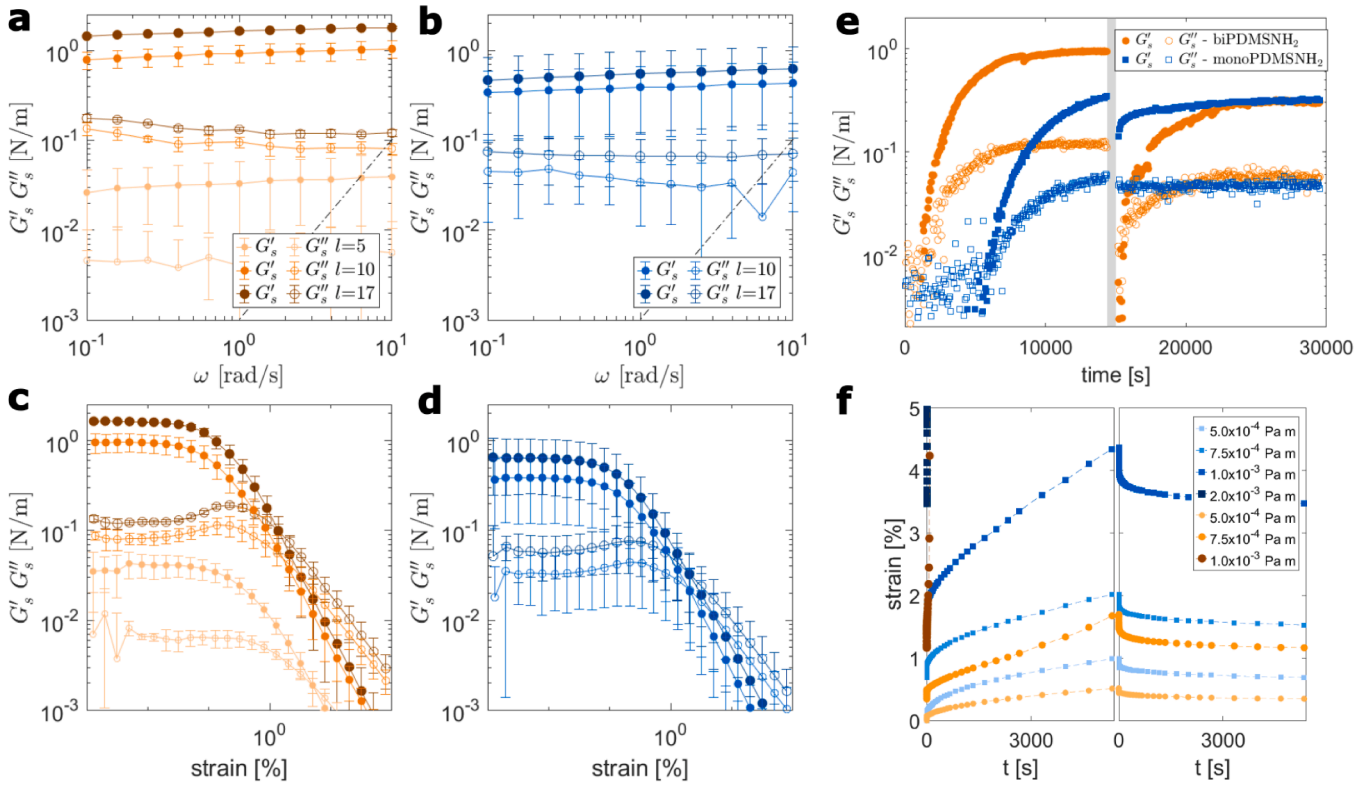

Fig. 2. (a-b) Interfacial shear frequency sweep for water-PDMS5 interfaces stabilized by MXenes and (a) biPDMSNH$_2$ or (b) monoPDMSNH$_2$ at strain 0.01%. (c-d) Interfacial shear amplitude sweep for water-PDMS5 interfaces stabilized by MXenes and (c) biPDMSNH$_2$ or (d) monoPDMSNH$_2$ at 1 rad/s. (e) Interfacial shear thixotropy test for water-PDMS5 interfaces stabilized by MXenes (l = 17) and biPDMSNH$_2$ (orange circles) or monoPDMSNH$_2$ (blue squares). First, an oscillation with an amplitude of 0.01% was applied for 4 hours to not interfere with the assembly of the particle network. Then, a 1 s^{-1} continuous shear was applied for 5 minutes to break the network (grey region). Finally, the interfacial network recovery was monitored at 0.01% strain for another 4 hours. (f) Creep and recovery curves of water-PDMS5 interfaces stabilized by MXene (l = 17) and biPDMSNH$_2$ (orange circles) or monoPDMSNH$_2$ (blue squares). The interfacial shear stress ranges between $5.0 \cdot 10^{-4}$ and $1.0 \cdot 10^{-3}$ $Pa \cdot m$.

PDMS. To overcome this limitation, the water-PDMS5 interface was visualized *in situ* using confocal reflection microscopy. Fig. 1e and f show the interfacial networks at the highest MXene concentration. Although single nanosheets cannot be resolved, clear differences in clustering are evident: MXene-biPDMSNH$_2$ forms larger, more interconnected agglomerates, while MXene-monoPDMSNH$_2$ produces smaller, less connected flocs. These observations support the hypothesis that biPDMSNH$_2$ promotes intersheet bridging, yielding a more cohesive interfacial network.

3.2. Interfacial shear rheology

After measuring the evolution of the interfacial shear moduli over time, the frequency and strain-dependent properties of the interfacial network have been determined. Measurements on plain water-oil interfaces and on surfactant-only interfaces showed an inertia-dominated response, confirming that neither component alone imparts measurable viscoelasticity. When MXenes are added to the water phase, both G'_s and G''_s increase over time (Fig. 1c-d). At steady state, the interface has a gel-like behavior with a storage modulus about an order of magnitude higher than the loss modulus and only weak frequency dependence (Fig. 2a and b). The viscoelastic moduli increase with particle concentration and, for $l \geq 10$, reach values comparable to those reported by Kamkar et al. for GO-stabilized interfaces, despite much lower bulk particle loadings (around 100 times lower in weight fraction) [23]. Additionally, the moduli of MXene-monoPDMSNH$_2$ interfaces are slightly lower than those of MXene-biPDMSNH$_2$ interfaces with the same particle concentration. This likely results from enhanced network connectivity provided by the double amino terminations of biPDMSNH$_2$, which reinforce particle interactions.

The effect of the applied strain on the interfacial network is shown in Fig. 2c-d and Table 2. For interfaces stabilized by biPDMSNH$_2$, the LVE region slightly reduces as particle concentration increases (Table 2), indicating that the network becomes more brittle at higher particle concentration.

As shown by Popple et al. [48], a higher bulk particle concentration leads to a thicker interfacial film but also introduces more roughness leading to a heterogeneous film. This might induce the formation of bigger agglomerates at the interface with few weak connection points generated by thinner nanosheet layers or surfactant molecules that create bridges between nanosheets. These connection points are relatively short (PDMSNH$_2$ chain length around 2 nm) and, therefore, make the interfacial network more brittle under shear. In contrast, monoPDMSNH$_2$-stabilized interfaces show nearly constant critical and flow strains across the accessible concentration range, suggesting that the interparticle interactions do not significantly change once coverage saturation is reached. While the critical and flow stress are lower than those of MXene-biPDMSNH$_2$, the critical and flow strain are slightly higher, indicating a less brittle interface.

Differences in network mechanics are also reflected in the G''_s response. For $l \geq 10$, G''_s presents a clear overshoot for MXene-biPDMSNH$_2$ interfaces, while a less pronounced G''_s overshoot is present in MXene-monoPDMSNH$_2$ interfaces. The G''_s overshoot has often been associated with network rearrangements and viscous energy dissipation [50]. In MXene-biPDMSNH$_2$ interfaces, the overshoot probably originates from rearrangements of nanosheet agglomerates and partial breakup of the nanosheet-surfactant interactions. Lastly, when

Table 2
Strain (γ) and stress (σ) values at the yield (c) and flow point (f). Data calculated from interfacial shear amplitude sweeps.

Surfactant	l [-]	γ_c [%]	σ_c [N/m]	γ_f [%]	σ_f [N/m]
biPDMSNH$_2$	5	0.12 ± 0.01	4.55 ±1.09 · 10^{-5}	6.15 ±0.69	1.25 ±0.39 · 10^{-4}
	10	0.05 ±0.00	3.79±0.80 · 10^{-4}	1.65 ±0.48	1.26±0.38 · 10^{-3}
	17	0.06±0.01	7.87±2.06 · 10^{-4}	1.42 ±0.68	2.00±0.46 · 10^{-3}
monoPDMSNH$_2$	10	0.06 ±0.01	1.97 ±1.05 · 10^{-4}	2.00 ±0.40	6.24±3.80 · 10^{-4}
	17	0.06 ±0.02	3.70 ±2.20 · 10^{-4}	1.83 ±0.53	0.98±0.55 · 10^{-3}

comparing normalized stress $\bar{\sigma} = \sigma/\sigma_0$ versus strain amplitude (Fig. S11), the two types of MXene-surfactant complexes also exhibit different behaviors. As the interfacial response starts to deviate from the linear behavior, MXene-monoPDMSNH$_2$ interfaces hold a slightly higher residual stiffness with $\bar{\sigma}$ higher than the one of MXene-biPDMSNH$_2$ interfaces.

Creep experiments at $l = 17$ further highlight the differences between the two systems (Fig. 2f and Fig. S12). Both interfacial structures show viscoelastic behavior with incomplete strain recovery. Moreover, when applying the same stress, the resulting deformation is higher for the interface stabilized by monoPDMSNH$_2$ compared to that with biPDMSNH$_2$, in agreement with the amplitude sweep results where the moduli of MXene-biPDMSNH$_2$ interfaces are slightly higher than those of MXene-monoPDMSNH$_2$ interfaces with the same particle concentration. Nonetheless, the interface has an earlier transition to viscous behavior in the biPDMSNH$_2$ sample than in the monoPDMSNH$_2$, suggesting that biPDMSNH$_2$-stabilized interfaces have a lower yield stress under shear flow than those stabilized by monoPDMSNH$_2$. This is in contrast with the results from the amplitude sweep, where the critical stress is higher for interfaces stabilized by biPDMSNH$_2$ compared to monoPDMSNH$_2$, suggesting that nanosheet-nanosheet and nanosheet-surfactant interactions respond differently under oscillatory versus continuous shear.

Thixotropy measurements (Fig. 2e) also reflect structural differences. After network disruption at a shear rate of 1 s^{-1}, the interface stabilized by MXenes and monoPDMSNH$_2$ recovered almost completely and within a few minutes, while MXene-biPDMSNH$_2$ interfaces exhibited only a partial recovery, requiring a much longer time. A proposed mechanism is that, when shearing the MXene-biPDMSNH$_2$ network, both side-side nanosheet interactions and the surfactant-mediated bridges linking adjacent nanosheets are progressively weakened and eventually disrupted. When the interfacial network recovers, only side-side interactions are completely restored, while the surfactant bridges are partially lost. This would explain why both surfactants show similar viscoelasticity at the end of the recovery curves. Additionally, larger interfacial agglomerates in the MXene-biPDMSNH$_2$ system (Fig. 1c) likely prolong the time required to reorganize into a homogeneous structure, explaining the slower recovery.

3.3. Interfacial dilatational rheology

Oscillatory tests were performed on a pendant drop tensiometer with a piezoelectric unit (ThetaFlex, Biolin) to investigate the response to small dilatational deformations. Fig. 3a and b show that, similar to the shear measurements, the elastic dilatational modulus increases with particle concentration and exhibits only weak frequency dependence, consistent with a gel-like interfacial network. It is interesting to notice that, in the absence of MXenes, water-surfactant interfaces already show a weak viscoelastic behavior in dilatation with $E_s' \sim E_s''$ for water-biPDMSNH$_2$, and slightly higher E_s'' than E_s' for water-monoPDMSNH$_2$. The storage moduli follow a power law behavior ($E_s' \sim \omega^n$), where n is equal to 0.38 and 0.51 for water-biPDMSNH$_2$ and water-monoPDMSNH$_2$, respectively. According to the Lucassen-van den Tempel model, $n \approx 0.5$ indicates a dilatational response governed by surfactant exchange between bulk and interface [52]. As the particle concentration increases, n decreases markedly, reaching 0.04 and 0.16

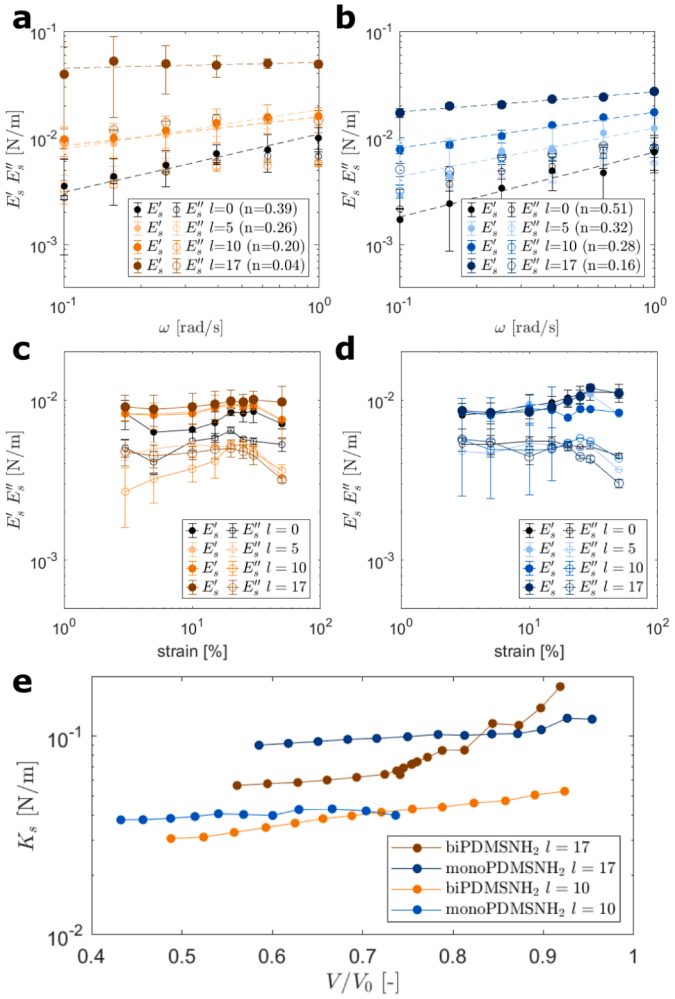

Fig. 3. (a-b) Interfacial dilatational frequency sweep for water-PDMS5 interfaces stabilized by MXene and (a) biPDMSNH$_2$ or (b) monoPDMSNH2 at strain 1%. Dashed lines indicate fits to a power-law function with exponent n. (c-d) Interfacial dilatational amplitude sweep for water-PDMS5 interfaces stabilized by MXene and (c) biPDMSNH$_2$ or (d) monoPDMSNH$_2$ at 0.05 Hz. (e) Compressional modulus K_s of water-PDMS5 interfaces stabilized by MXenes and biPDMSNH$_2$ or monoPDMSNH$_2$. The modulus was calculated using the capsule tensiometry algorithm developed by Hegemann et al. [51].

for water-biPDMSNH$_2$ and water-monoPDMSNH$_2$ at $l = 17$, respectively, and indicating the growing contribution of in-plane particle interactions to the viscoelastic response.

Overall, MXene-biPDMSNH$_2$ interfaces exhibit a slightly stronger response in dilatation compared to MXene-monoPDMSNH$_2$ ones, in line with the interfacial shear measurements. Nonetheless, the dilatational interfacial moduli are up to two orders of magnitude lower than the shear interfacial moduli, with $0.02 < |E_s^*|/|G_s^*| < 0.45$, resulting in negative Poisson ratios $\left(\nu = \frac{(E_s^* - G_s^*)}{(E_s^* + G_s^*)}\right) - 0.95 < \nu < -0.35$. Inter-

faces with negative Poisson ratio were previously observed by Alicke et al. [53]. In their study, the interfacial network exhibits an auxetic behavior due to the hinged rotation of particle aggregates. In our system, the negative Poisson ratio originates from the very low resistance of the MXene network to area dilation whereby particle-free interfacial areas are exposed, combined with partial nanosheet stacking during compression.

Amplitude sweep measurements (Fig. 3c,d) performed using a step-motor tensiometer (Tracker, Teclis) further illustrate this weak dilatational elasticity. At relatively large deformations, the dilatational viscoelastic response does not change significantly for different MXene coverages, and it is also very similar to the response of the interfaces covered only by surfactants. Furthermore, the deformation amplitude does not clearly affect the elastic and viscous moduli. It is important to notice that, in these tests, it was not possible to measure samples at the same amplitude used in the frequency sweeps since the step motor is not able to apply a purely sinusoidal deformation at strains lower than 3%. Large compressions promote nanosheet rearrangement into larger agglomerates (Fig. S13), reducing interfacial density and suppressing particle contributions to E_s' and E_s''. Therefore, these moduli represent the effective resistance of the MXene-covered interface to repeated area dilatation rather than a constitutive property of a continuous elastic network. Overall, these results confirm that the MXene networks resist shear deformations much more effectively than dilatational ones.

Despite the relatively constant dynamic moduli, it is worth mentioning that the intracycle behavior changes with the applied amplitude (Fig. S14). Lissajous plots show that cycles become asymmetric between compression and dilation as the strain increases, regardless of surfactant type. The origins of these non-linearities were further analyzed with the general stress decomposition (GSD) method developed by de Groot et al. [54] as shown in Fig. S15 and explained in detail in Section S4.1. This analysis reveals that the MXene-biPDMSNH$_2$ interfaces have a higher contribution of the surface density changes upon dilatation deformation than the MXene-monoPDMSNH$_2$ interfaces.

To further probe the effect of deformation on the dilatational elastic modulus with an independent method that focusses on the first deformation of the interface, we also analysed the droplet retraction using the pendant capsule tensiometry algorithm developed by Hegemann et al. (Section S4.2 and Fig. S16) [51]. This method provides the compressional dilatational modulus K_s directly from the shape evolution during retraction. The analysis was feasible only for $l \geq 10$, as droplets with lower interfacial coverage behave too close to a Young-Laplace surface for a reliable extraction of elastic contributions (Fig. 3e). The measured K_s values are slightly higher than the E_s' values obtained from oscillatory dilatation experiments. Importantly, the trends are consistent with the shear interfacial measurements: at small deformations (large V/V_0), MXene-biPDMSNH$_2$ exhibits a higher modulus than MXene-monoPDMSNH$_2$, whereas at larger deformations (lower V/V_0) the behavior reverses, and the MXene-monoPDMSNH$_2$ interfaces appear more resistant to compressional deformation. This crossover highlights that the two nanosheet-surfactant networks respond differently to dilatational strain, with biPDMSNH$_2$ forming initially stiffer but more deformation-sensitive structures, while monoPDMSNH$_2$ yields networks that withstand larger deformations. While Langmuir trough measurements could, in principle, provide deeper insight into interfacial dilatational behavior, this technique is not suitable for this system with a limited sensitivity of the surface presssure to area changes (Section S1.3 and Fig. S7), and a different material system would be required to investigate the dilatational response in more detail.

3.4. Droplet deformation

The behavior of a single droplet under shear flow was investigated for different flow conditions and with the various MXenes-covered interfaces discussed in Sections 3.1–3.3. Fig. 4a shows how the droplet shape evolves when increasing the Ca number for water droplets and MXene-covered droplets in PDMS60 with biPDMSNH$_2$. The same data are quantitatively represented by the relation between the dimensionless major axis $L' = L/2R$ and the capillary number in Fig. 4b–d.

A water droplet in the PDMS60 matrix combined with biPDMSNH$_2$ acts like a viscous droplet in a Newtonian matrix ($\lambda = \eta_{droplet}/\eta_{matrix} = 1.5 \cdot 10^{-5}$) starting to stretch as soon as a small shear (i.e. Ca number) is applied. After an initial linear increase of the major axis with the Ca number, L' increases faster until reaching a plateau at Ca$\geq$ 0.2. The droplet assumes a sigmoidal shape in this region with highly pronounced tips ($l = 0$ at Ca = 0.22 in Fig. 4a). This behavior is typical for droplets with a low viscosity ratio $\lambda < 0.1$ [55], where the shear flow generates a gradient of surfactant at the interface with accumulation of surfactants at the droplet tips, eventually leading to tip streaming breakup as small droplets begin to separate from the tips of the sigmoid. It is worth mentioning that the deformation curves for water droplets in PDMS60 with biPDMSNH$_2$ and monoPDMSNH$_2$ overlap with each other. This indicates that the behavior of interfaces stabilized only by surfactants can be adequately described by taking only their interfacial tension into account. As MXene nanosheets are added to the droplet phase at a low concentration ($l = 5$, Fig. 4a), the droplet initially acts similarly to a water droplet with $L' > 1$ as soon as a shear rate is applied. When Ca $\geq$ 0.1, the L'($l = 5$) curve starts to deviate significantly from the water droplet behavior. At Ca = 0.22, the water droplet stretches almost two times more than the $l = 5$ droplet and the latter keeps its ellipsoidal shape, arresting the formation of elongated tips. This is probably because the nanosheets create an interfacial viscoelastic network, leading to decreased mobility of the surfactant that no longer accumulates on the droplet tips. For higher particle coverages ($l = 10$ and $l = 17$, Fig. 4b and c), a solid-like behavior is observed at low Ca number as the droplets keep a quasi-spherical shape. When the Ca number exceeds a yielding value Ca_{yield}, the droplet begins to deform reaching an ellipsoidal shape with L' rapidly increasing with the shear rate $(Ca) \cdot Ca_{yield}$ increases with the surface coverage. This behavior has been typically observed in capsules with a purely elastic interface. Koleva et al. [56] found that this behavior is due to the non-perfectly symmetrical capsule shape and inhomogeneity of the interfacial layer that causes the droplet to rotate under flow but not significantly deform. This is very clearly the case for MXene-covered droplets ($l \geq 17$), since when highly nanosheet-loaded droplets are injected in the matrix the droplets do not have enough time to relax before the interfacial network is formed and, therefore, they stabilize into a non-perfectly spherical shape (Fig. 4a, $l = 17$, Ca = 0).

Similar observations can be made for droplets in PDMS60 with monoPDMSNH$_2$ of which the images can be found in Fig. S17. However, when comparing L' between the two surfactants, the droplets reach a smaller deformation for the same Ca number in a PDMS-monoPDMSNH$_2$ matrix compared to droplets with the same surface coverage stabilized by biPDMSNH$_2$ (Fig. 4e). Even though droplets stabilized with monoPDMSNH$_2$ are more resistant under shear flow, the corresponding Ca_{yield} is similar to the one of biPDMSNH2-stabilized droplets. Once $Ca > Ca_{yield}$, L' slowly increases with the Ca number, leading to a lower deformation than that of the biPDMSNH$_2$-stabilized droplets. These differences can be a result of the different shear response of the interfacial network as seen in Section 3.2. Since the interfacial MXene network has a low resistance to dilatation, its dilatational viscoelasticity plays only a small role in suppressing droplet deformation. This also agrees with theoretical models, such as the one of Yu et al. [33], in which only the dilatational and shear interfacial viscosities are considered to investigate droplet dynamics under shear flow. Their results indicate that droplet deformation is significantly suppressed only when the ratio of dilatational to shear interfacial viscosity is lower than one. Therefore, interfaces with stronger resistance in shear than in dilatation can more effectively inhibit the droplet deformation.

In terms of interfacial shear viscoelasticity, the two interfacial systems have similar properties in the linear regime, which also explains why droplets stabilized by the two different surfactants have com-

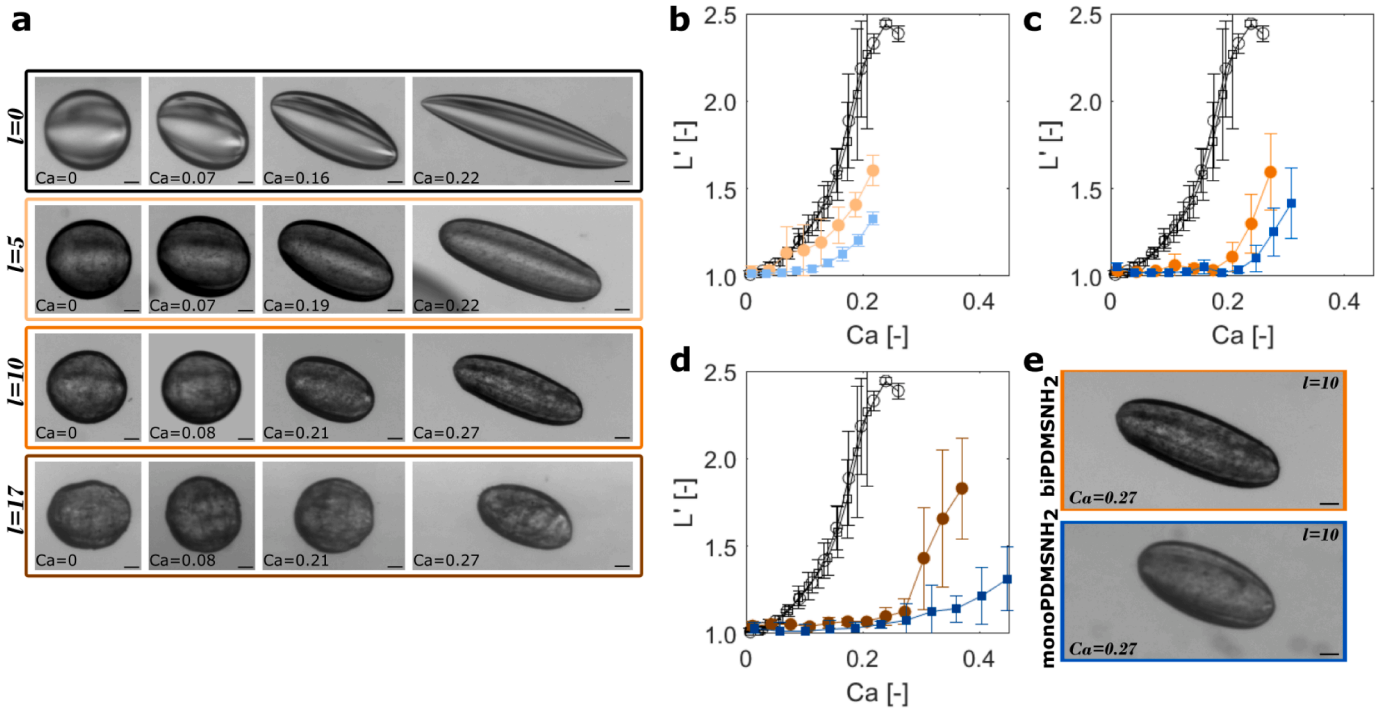

Fig. 4. (a) Steady state droplet deformation at increasing Ca numbers for water and MXenes-filled droplets in PDMS60 matrix with biPDMSNH$_2$. Scale bar: 100 μm. (b-d) Non-dimensional droplet length L' versus Ca number for MXene-filled droplets in PDMS60 with biPDMSNH$_2$ (orange circles) and monoPDMSNH$_2$ (blue squares) at (b) l = 5 (c) l = 10 (d) l = 17. The empty symbols correspond to water droplets in PDMS60 with biPDMSNH$_2$ (circles) and monoPDMSNH$_2$ (squares). (e) Sheared MXene-filled droplet (l = 10) in PDMS60 with biPDMSNH$_2$ (top) and monoPDMSNH$_2$ (bottom) at Ca = 0.27.

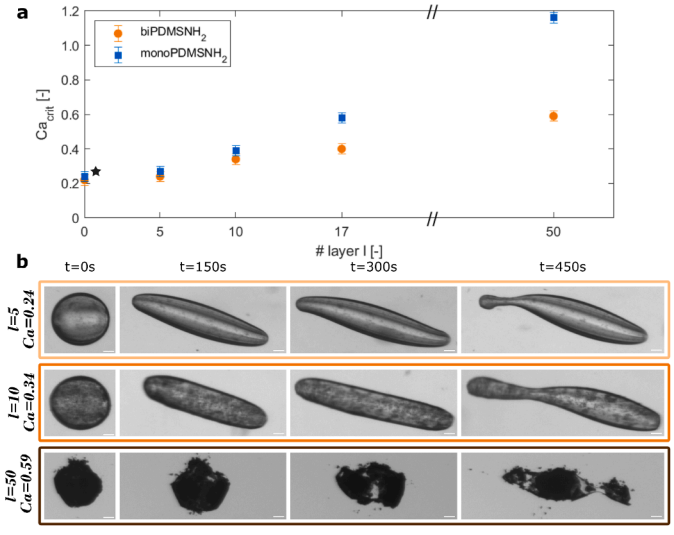

Fig. 5. Dynamics of droplet breakup. (a) Ca_{crit} vs theoretical number of layers l. The Ca_{crit} for l = 0(⋆) has been selected as the Ca at which the tip streaming starts. (b) Images of droplet deformation at Ca_{crit} for l = 5, l = 10 and l = 50 in PDMS60 with biPDMSNH$_2$.

parable Ca_{yield}. Nonetheless, as discussed in Section 3.2, the two interfaces behave differently in the non-linear regime, which also corresponds to the region where the droplets exhibit distinct responses under shear. MXenes-monoPDMSNH$_2$ interfaces preserve a higher retained stress beyond the yield point (Fig. S11) and present a less brittle network, as shown in Fig. 2f. These distinct non-linear interfacial properties play a key role in governing droplet behavior at $Ca > Ca_{yield}$. Hence, after Ca_{yield}, the interfacial network becomes weaker for MXene-biPDMSNH$_2$ droplets, leading to higher droplet deformation compared to MXene-monoPDMSNH$_2$ systems.

It should be noted that this post-yield response does not correspond to a purely nonlinear viscoelastic behavior of an intact, homogeneous interface. Instead, deformation beyond yield is accompanied by irreversible nanosheet rearrangement and progressive disruption of the interfacial network, as evidenced by the incomplete recovery of the interfacial shear modulus in Fig. 2e and the fact that the droplet deformation is enhanced if the droplet has already been subjected to a higher Ca number (Fig. S18). This deformation hysteresis was also observed by Mei et al. for silica-coated droplets [29]. Consequently, the post-yield behavior reflects a reduction in interfacial load-bearing capability rather than a reversible nonlinear elastic constitutive response, highlighting the need for droplet deformation models that incorporate yielding and deformation-induced interfacial restructuring.

3.5. Droplet breakup

When the Ca number exceeds a critical value Ca_{crit}, the droplet deforms irreversibly until breakup. The breakup dynamics are highly dependent on the interfacial network and surface coverage, as shown in Fig. 5a and b for a PDMS-biPDMSNH$_2$ matrix. For water droplets, as reported in the previous section, it is difficult to identify a clear breakup point. However, for Ca≥ 0.2 the droplet reaches a stable sigmoidal shape that keeps the same L' even when increasing the Ca number. Similar to the droplet deformation trend, monoPDMSNH$_2$-stabilized droplets can be sheared until higher Ca numbers before undergoing breakup for all three concentrations of MXenes, which was already attributed to the non-linear interfacial shear rheological behavior (Section 3.4). In general, as shown in Fig. 5a, Ca_{crit} increases with increasing particle concentration. At l = 5, the droplet first assumes a shape similar to a sigmoid with rounder tips. Afterward, small droplets, with a radius approximately 10 times smaller than that of the original droplet and a jammed interface, separate from the tips. This occurs because, initially, the interfacial network arrests the formation of a surfactant gradient between the center and the sides of the droplet. However, at high Ca numbers, the interfacial network starts to break, turning into a liquid-

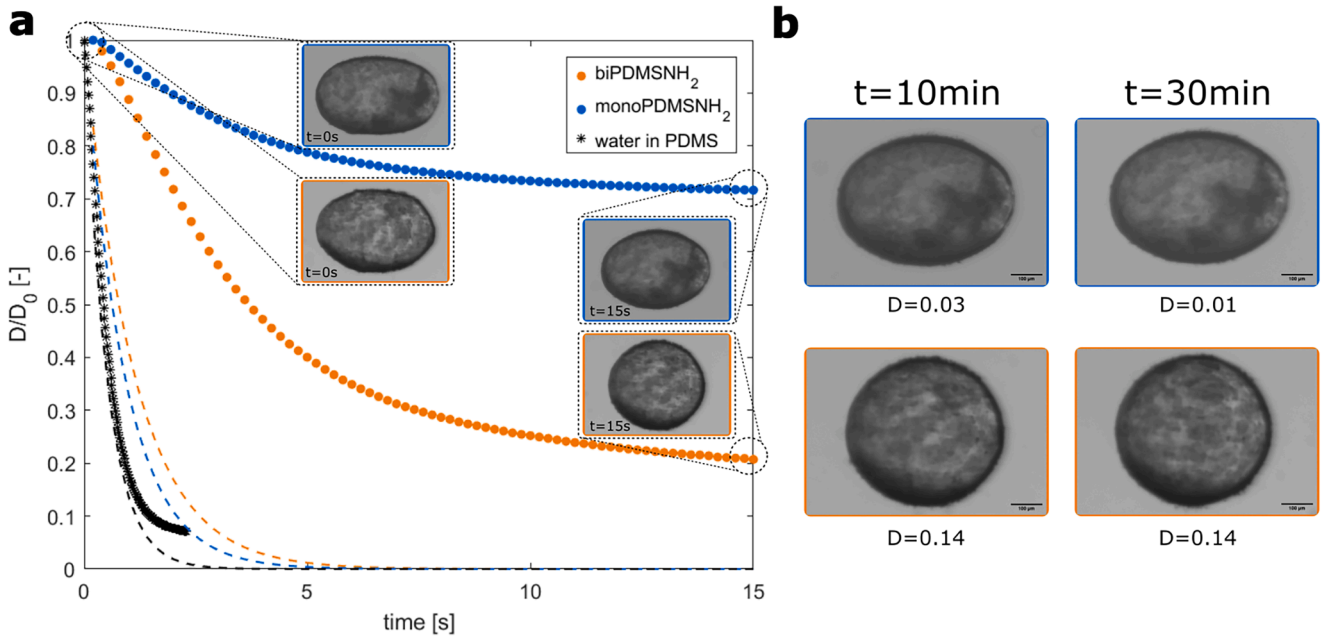

Fig. 6. (a) Evolution over time of droplet deformation after flow cessation with $L_{P_0}/2R = 1.27$ for all cases. The symbols represent experimental data, while the dotted lines represent the droplet deformation evolution according to the Luciani's model [57]. (b) Images of droplets 10 and 30 minutes after flow cessation (biPDMSNH$_2$ in orange frame, monoPDMSNH$_2$ in blue frame).

like interface and nanosheets-surfactant agglomerates accumulate at the extremities of the droplet due to the applied shear. At $l \geq 10$, the droplet breaks into two droplets of similar size. As suggested from the interfacial shear rheology data, this higher surface coverage and elastic modulus lead to a breakup of the interfacial network into bigger agglomerates that prevent the formation of elongated tips. Finally, we also examined the case of a droplet loaded with a higher particle concentration than the one tested so far, $l = 50$. It was not possible to accurately quantify the deformation behavior for this surface coverage since the initial droplet shape largely deviates from a sphere (Fig. S19). Due to the high load of particles, once formed, the droplet does not have enough time to completely relax to a spherical shape due to the interfacial elastic network formation that jams the droplet into a disk-like shape. In this case, when $Ca \geq Ca_{crit}$, the interfacial network undergoes severe instabilities, as also visible from Fig. 5b, where the interfacial network starts to visibly crack, after which several flocks separate leading to the formation of two or more daughter droplets. A similar mechanism was found by Mei et al. [29] for particle-covered PDMS droplets in a PIB matrix. In their case, the droplet interface is left for several days to form a stable particle network before showing such instabilities during break up. In both cases, the droplet irregularities are generated by the cracking of the viscoelastic network, creating interfacial discontinuity and, therefore, separation in multiple droplets.

3.6. Droplet retraction

The behavior of MXene-covered droplets after flow cessation was investigated to probe the retraction dynamics. Fig. 6 shows the evolution of the nondimensional droplet deformation D/D_0 after flow cessation for $l = 10$ aqueous droplets with biPDMSNH$_2$ and monoPDMSNH$_2$, where $D = (L - B)/(L + B)$. The two systems behave significantly differently even though the initial droplet nondimensional length is similar ($L_{P_0'} \simeq 1.27$). After stopping the flow, the droplet sheared in PDMS60 with biPDMSNH$_2$ matrix has an almost complete retraction to a spherical shape with $D = 0.01$ after 30 mins, while the droplet stabilized by monoPDMSNH$_2$ keeps a residual deformation of $D = 0.14$ even 30 minutes after the flow has been stopped. A reason for this difference can be found in the ability of the system to restore its network after shear. As Fig. 2e shows, once the MXene-surfactant network is broken, the interface requires a longer time to rebuild its viscoelasticity when biPDMSNH$_2$ is used in the oil phase. Additionally, while the MXene-monoPDMSNH$_2$ network recovers completely to its original viscoelastic properties, the MXene-biPDMSNH$_2$ network recovers only partially. This could mean that, while the droplet is retracting, the nanosheet-monoPDMSNH$_2$ network is quickly restored, jamming the interface and locking it into a deformed state. On the other hand, the nanosheet-biPDMSNH$_2$ network rebuilds significantly slower than the droplet retraction kinetics returning to a spherical shape. In other words, the steady state droplet shape is determined by the balance between the retraction kinetics of the droplet and the recovery kinetics of the interfacial network [37,58]. This is further confirmed by comparing these results with Luciani's model for droplet retraction [57]. According to the model, the evolution of the droplet deformation after flow cessation can be described by the equation:

$$D/D_0 = exp(-\frac{40(\lambda+1)}{(2\lambda+3)(19\lambda+16)}\frac{\Gamma}{\eta R_0}) \quad (1)$$

The model predicts well the retraction kinetics of a plain water droplet in PDMS60 but overestimates the retraction speed for particle-covered droplets. This is because the interfacial tension Γ is considered in the equation as the only stress applied to the droplet during retraction and the stresses generated by the interfacial elasticity are neglected.

4. Conclusions

In this study, we present the first investigation of the interfacial rheological properties of MXene-covered interfaces and their impact on droplet dynamics. MXene nanosheets have raised great interest as Pickering emulsion stabilizers in recent years, mainly due to their excellent conductive properties [9,12,20,22,46]. A promising strategy to assemble MXenes at water-oil interfaces involves electrostatic interactions with oppositely charged surfactants dispersed in the oil phase. These systems have been used for fabrication of emulsion-templated conductive composites and liquid-in-liquid printing for reconfigurable electronics [9,22]. However, the interfacial rheological properties of MXene-covered interfaces have not been explored yet.

Our results show that the interfacial rheological response is highly sensitive to the number of charged head groups in the surfactant. By comparing MXene-biPDMSNH$_2$ and MXene-monoPDMSNH$_2$ complexes, we demonstrate that both systems exhibit strong shear viscoelasticity but relatively weak dilatational elasticity. MXene-biPDMSNH$_2$ complexes generate a more interconnected network, which enhances interfacial viscoelasticity but leads to large agglomerates that are more susceptible to irreversible breakup under shear flow. Conversely, MXene-monoPDMSNH$_2$ complexes produce a more flexible and homogeneous interfacial layer that retains stiffness in the non-linear regime and recovers more rapidly after shear.

Our single-droplet experiments highlight that nonlinear interfacial mechanics, rather than the linear viscoelastic modulus, govern droplet deformation under flow. Unlike droplets stabilized by spherical particles, which deform monotonically with capillary number [28,29], MXene-covered droplets behave like soft solids when $Ca \leq Ca_{yield}$, similar to capsules with elastic membranes [56]. Furthermore, MXene-biPDMSNH$_2$ droplets deform more and break at lower Ca compared to MXene-monoPDMSNH$_2$ droplets, underscoring the role of nonlinear, deformation- and deformation-history dependent interfacial stresses rather than intrinsic linear moduli in setting droplet behavior. These trends cannot be captured by existing analytical droplet deformation models that rely on linear interfacial properties or assume a direct correspondence between viscoelastic moduli and deformation [32,35]. Our results, therefore, highlight the need for droplet deformation models that explicitly incorporate interfacial yielding and deformation-induced restructuring, as beginning to be addressed in recent numerical simulations of droplet dynamics [59] and interfacial constitutive frameworks [60].

While the present study focuses on interfacial mechanics and droplet deformation, the insights gained are directly relevant to systems where both mechanical stability and functional performance, such as electrical conductivity, are critical. Examples include MXene-based composites for EMI shielding, soft electronics, or sensing applications [9,12,22]. Building on these findings, future work will aim to formulate conductive Pickering emulsions and evaluate how the interfacial network and resulting macroscopic structure influence their rheological properties and conductive pathways.

Declaration of Generative AI and AI-assisted technologies in the writing process

During the preparation of this work the authors used ChatGPT in order to polish the sentence structure and grammar. After using this tool, the authors reviewed and edited the content and take full responsibility for the content of the publication.

CRediT authorship contribution statement

Benedetta Attaianese: Writing – original draft, Visualization, Methodology, Investigation, Formal analysis, Conceptualization; **Gangamallaiah Velpula:** Investigation, Formal analysis; **Jennifer Theissen:** Investigation, Formal analysis; **Leonard M.C. Sagis:** Supervision, Resources; **Ruth Cardinaels:** Writing – review & editing, Supervision, Funding acquisition, Conceptualization.

Data availability

Data will be made available on request.

Declaration of competing interest

The authors declare the following financial interests/personal relationships which may be considered as potential competing interests: Ruth Cardinaels reports financial support was provided by European Research Council. Ruth Cardinaels reports financial support was provided by Internal Funds KU Leuven. Gangamallaiah Velpula reports financial support was provided by Research Foundation Flanders. Jennifer Theissen reports financial support was provided by Research Foundation Flanders. If there are other authors, they declare that they have no known competing financial interests or personal relationships that could have appeared to influence the work reported in this paper.

Acknowledgements

This work has received funding from Internal Funds KU Leuven under project number STG/20/035 and was supported by funding from the European Research Council (ERC) under the European Union's Horizon 2020 research and innovation programme: Grant Agreement No. 948739 – PEM-SPrint. G.V. thanks the support of KU Leuven - Internal Funds (C14/23/090), and FWO (G0A3220N). J.T. thanks the support of the FWO and F.R.S.-FNRS (Belgium) under the Excellence of Science (EOS) program ("PHOSPORE" - EOS reference No: 40,007,504). The authors thank Rik Nuyts (KU Leuven, Department of Chemistry) for the SEM-EDX measurements.

Supplementary material

Supplementary material associated with this article can be found, in the online version, at 10.1016/j.jcis.2026.140182

References

[1] Z. Wang, S. Huang, X. Zhao, S. Yang, K. Mai, W. Qin, K. Liu, J. Huang, Y. Feng, J. Li, et al., Covalent bond interfacial recognition of polysaccharides/silica reinforced high internal phase Pickering emulsions for 3D printing, ACS Appl. Materi. Interfaces 15 (19) (2023) 23989–24002.
[2] J.H.J. Thijssen, J. Vermant, Interfacial rheology of model particles at liquid interfaces and its relation to (bicontinuous) Pickering emulsions, J. Physi. Condensed Matter 30 (2) (2017) 023002.
[3] A. Shi, X. Feng, Q. Wang, B. Adhikari, Pickering and high internal phase Pickering emulsions stabilized by protein-based particles: a review of synthesis, application and prospective, Food Hydrocolloids 109 (2020) 106117.
[4] M. Destribats, M. Eyharts, V. Lapeyre, E. Sellier, I. Varga, V. Ravaine, V. Schmitt, Impact of pNIPAM microgel size on its ability to stabilize Pickering emulsions, Langmuir 30 (7) (2014) 1768–1777.
[5] I. Kalashnikova, H. Bizot, P. Bertoncini, B. Cathala, I. Capron, Cellulosic nanorods of various aspect ratios for oil in water Pickering emulsions, Soft Matter 9 (3) (2013) 952–959.
[6] D.G. Ortiz, C. Pochat-Bohatier, J. Cambedouzou, M. Bechelany, P. Miele, Pickering emulsions stabilized with two-dimensional (2D) materials: a comparative study, Colloids Surfaces A: Physicochem. Eng. Aspects 563 (2019) 183–192.
[7] H. Jiang, Y. Sheng, T. Ngai, Pickering emulsions: Versatility of colloidal particles and recent applications, Current Opinion Colloid Interface Sci. 49 (2020) 1–15.
[8] S. De Smedt, B. Attaianese, R. Cardinaels, Direct ink writing of particle-based multiphase materials: From rheology to functionality, Current Opinion Colloid Interface Sci. 75 (2025) 101889.
[9] L. Li, Z. Deng, M. Chen, Z.-Z. Yu, T.P. Russell, H.-B. Zhang, 3D printing of ultralow-concentration 2D nanomaterial inks for multifunctional architectures, Nano Lett. 23 (1) (2022) 155–162.
[10] S.-M. Cui, S. Hashmi, W.-Q. Li, S. Handschuh-Wang, C.-T. Zhu, S.-C. Wang, Y.-F. Huang, G.-M. Zhu, F.J. Stadler, Rheology of graphene oxide stabilized Pickering emulsions, Soft Matter 19 (24) (2023) 4536–4548.
[11] Y. Zhang, G. Zhu, B. Dong, F. Wang, J. Tang, F.J. Stadler, G. Yang, S. Hong, F. Xing, Interfacial jamming reinforced Pickering emulgel for arbitrary architected nanocomposite with connected nanomaterial matrix, Nature commun. 12 (1) (2021) 111.
[12] Z. Zheng, Y. Zhao, Z. Ye, J. Hu, H. Wang, Electrically conductive porous MXene-polymer composites with ultralow percolation threshold via Pickering high internal phase emulsion templating strategy, J. Colloid Interface Sci. 618 (2022) 290–299.
[13] A. Alicke, S. Simon, J. Sblom, J. Vermant, Assessing the interfacial activity of insoluble asphaltene layers: Interfacial rheology versus interfacial tension, Langmuir 36 (49) (2020) 14942–14959.
[14] A.J. Mendoza, E. Guzmán, F. Martínez-Pedrero, H. Ritacco, R.G. Rubio, F. Ortega, V.M. Starov, R. Miller, Particle laden fluid interfaces: dynamics and interfacial rheology, Adv. Colloid Interface Sci. 206 (2014) 303–319.
[15] B. Madivala, J. Fransaer, J. Vermant, Self-assembly and rheology of ellipsoidal particles at interfaces, Langmuir 25 (5) (2009) 2718–2728.
[16] J.R. Samaniuk, Dynamics & rheology of 2d particles at fluid-fluid interfaces, Current Opinion Colloid Interface Sci. (2024) 101857.
[17] V.E. Blair, K. Celebi, K. Müllen, J. Vermant, Electrically conductive thin films derived from bulk graphite and liquid–liquid interface assembly, Adv. Mater. Interfaces 6 (4) (2019) 1801570.
[18] D.I. Petukhov, A.P. Chumakov, A.S. Kan, V.A. Lebedev, A.A. Eliseev, O.V. Konovalov, A.A. Eliseev, Spontaneous MXene monolayer assembly at the liquid–air interface, Nanoscale 11 (20) (2019) 9980–9986.

[19] L. Imperiali, K.-H. Liao, C. Clasen, J. Fransaer, C.W. Macosko, J. Vermant, Interfacial rheology and structure of tiled graphene oxide sheets, Langmuir 28 (21) (2012) 7990–8000.
[20] R. Bian, R. Lin, G. Wang, G. Lu, W. Zhi, S. Xiang, T. Wang, P.S. Clegg, D. Cai, W. Huang, 3D assembly of Ti 3 C 2-MXene directed by water/oil interfaces, Nanoscale 10 (8) (2018) 3621–3625.
[21] S. Zhao, L. Li, H.-B. Zhang, B. Qian, J.-Q. Luo, Z. Deng, S. Shi, T.P. Russell, Z.-Z. Yu, Janus MXene nanosheets for macroscopic assemblies, Mater. Chem. Front. 4 (3) (2020) 910–917.
[22] J.D. Cain, A. Azizi, K. Maleski, B. Anasori, E.C. Glazer, P.Y. Kim, Y. Gogotsi, B.A. Helms, T.P. Russell, A. Zettl, Sculpting liquids with two-dimensional materials: the assembly of Ti3C2T x MXene sheets at liquid–liquid interfaces, ACS Nano 13 (11) (2019) 12385–12392.
[23] M. Kamkar, E. Erfanian, P. Bazazi, A. Ghaffarkhah, F. Sharif, G. Xie, A. Kannan, M. Arjmand, S.H. Hejazi, T.P. Russell, et al., Interfacial assembly of graphene oxide: from super elastic interfaces to liquid-in-liquid printing, Adv. Mater. Interfaces 9 (6) (2022) 2101659.
[24] A. Alicke, J. Vermant, Yielding of model particle-laden interfaces in shear and compression, Rheologica Acta 64 (9) (2025) 583–600.
[25] S.F. Velandia, D. Ramos, M. Lebrun, P. Marchal, C. Lemaitre, V. Sadtler, T. Roques-Carmes, Exploring the link between interfacial and bulk viscoelasticity in reverse Pickering emulsions, Colloids Surfaces A Physicochem. Eng. Aspects 624 (2021) 126785.
[26] G.I. Taylor, The viscosity of a fluid containing small drops of another fluid, Proc. R. Soc. London. Series A, Containing Papers Math. Phys. Character 138 (834) (1932) 41–48.
[27] P.L. Maffettone, M. Minale, Equation of change for ellipsoidal drops in viscous flow, J. Non-Newtonian Fluid Mech. 78 (2-3) (1998) 227–241.
[28] M. Kaganyuk, A. Mohraz, Shear-induced deformation and interfacial jamming of solid-stabilized droplets, Soft Matter 16 (18) (2020) 4431–4443.
[29] Y. Mei, G. Li, P. Moldenaers, R. Cardinaels, Dynamics of particle-covered droplets in shear flow: unusual breakup and deformation hysteresis, Soft Matter 12 (47) (2016) 9407–9412.
[30] R. Chachanidze, K. Xie, J. Lyu, M. Jaeger, M. Leonetti, Breakups of Chitosan microcapsules in extensional flow, J. Colloid Interface Sci. 629 (2023) 445–454.
[31] L. Bécu, L. Benyahia, Strain-induced droplet retraction memory in a pickering emulsion, Langmuir 25 (12) (2009) 6678–6682.
[32] C.-X. Zhao, E. Rondeau, J.J. Cooper-White, A.P.J. Middelberg, Microfluidic elucidation of the effects of interfacial rheology on droplet deformation, Ind. Eng. Chem. Res. 51 (4) (2012) 2021–2029.
[33] W. Yu, C. Zhou, Dynamics of droplet with viscoelastic interface, Soft Matter 7 (13) (2011) 6337–6346.
[34] R.W. Flumerfelt, Effects of dynamic interfacial properties on drop deformation and orientation in shear and extensional flow fields, J. Colloid Interface Sci. 76 (2) (1980) 330–349.
[35] P. Erni, E.J. Windhab, P. Fischer, Emulsion drops with complex interfaces: globular versus flexible proteins, Macromolecul. Mater. Eng. 296 (3-4) (2011) 249–262.
[36] J. Smits, R.P. Giri, C. Shen, D. Mendonca, B. Murphy, P. Huber, K. Rezwan, M. Maas, Synergistic and competitive adsorption of hydrophilic nanoparticles and oil-soluble surfactants at the oil–water interface, Langmuir 37 (18) (2021) 5659–5672.
[37] M. Cui, T. Emrick, T.P. Russell, Stabilizing liquid drops in nonequilibrium shapes by the interfacial jamming of nanoparticles, Science 342 (6157) (2013) 460–463.
[38] C. Huang, M. Cui, Z. Sun, F. Liu, B.A. Helms, T.P. Russell, Self-regulated nanoparticle assembly at liquid/liquid interfaces: a route to adaptive structuring of liquids, Langmuir 33 (32) (2017) 7994–8001.
[39] A. Toor, J. Forth, S. Bochner de Araujo, M.C. Merola, Y. Jiang, X. Liu, Y. Chai, H. Hou, P.D. Ashby, G.G. Fuller, T.P. Russell, Mechanical properties of solidifying assemblies of nanoparticle surfactants at the oil–water interface, Langmuir 35 (41) (2019) 13340–13350.
[40] M. Alhabeb, K. Maleski, B. Anasori, P. Lelyukh, L. Clark, S. Sin, Y. Gogotsi, Guidelines for synthesis and processing of two-dimensional titanium carbide (Ti3C2Tx MXene), Chem. Mater. 29 (2017) 7633–7644.
[41] K. Maleski, C.E. Ren, M.-Q. Zhao, B. Anasori, Y. Gogotsi, Size-dependent physical and electrochemical properties of two-dimensional MXene flakes, ACS Appl. Mater. Interfaces 10 (29) (2018) 24491–24498.
[42] B. Akuzum, K. Maleski, B. Anasori, P. Lelyukh, N.J. Alvarez, E.C. Kumbur, Y. Gogotsi, Rheological characteristics of 2D titanium carbide (MXene) dispersions: a guide for processing MXenes, ACS Nano 12 (3) (2018) 2685–2694.
[43] S. Vandebril, A. Franck, G.G. Fuller, P. Moldenaers, J. Vermant, A double wall-ring geometry for interfacial shear rheometry, Rheologica Acta 49 (2010) 131–144.
[44] A. Vananroye, P. Van Puyvelde, P. Moldenaers, Effect of confinement on droplet breakup in sheared emulsions, Langmuir 22 (9) (2006) 3972–3974.
[45] J.S. Vrentas, D.C. Venerus, C.M. Vrentas, An exact analysis of reservoir effects for rotational viscometers, Chem. Eng. Sci. 46 (1) (1991) 33–37.
[46] H. Cao, M. Escamilla, K.D. Arole, D. Holta, J.L. Lutkenhaus, M. Radovic, M.J. Green, E.B. Pentzer, Flocculation of MXenes and their use as 2D particle surfactants for capsule formation, Langmuir 37 (8) (2021) 2649–2657.
[47] Z. Sun, T. Feng, T.P. Russell, Assembly of graphene oxide at water/oil interfaces: tessellated nanotiles, Langmuir 29 (44) (2013) 13407–13413.
[48] D. Popple, M. Shekhirev, C. Dai, P. Kim, K.X. Wang, P. Ashby, B.A. Helms, Y. Gogotsi, T.P. Russell, A. Zettl, All-liquid reconfigurable electronics using jammed MXene interfaces, Adv. Mater. 35 (13) (2023) 2208148.
[49] B. Wu, C. Yang, Q. Xin, L. Kong, M. Eggersdorfer, J. Ruan, P. Zhao, J. Shan, K. Liu, D. Chen, et al., Attractive Pickering emulsion gels, Adv. Mater. 33 (33) (2021) 2102362.
[50] G.J. Donley, P.K. Singh, A. Shetty, S.A. Rogers, Elucidating the G overshoot in soft materials with a yield transition via a time-resolved experimental strain decomposition, Proc. Nat. Acad. Sci. 117 (36) (2020) 21945–21952.
[51] J. Hegemann, S. Knoche, S. Egger, M. Kott, S. Demand, A. Unverfehrt, H. Rehage, J. Kierfeld, Pendant capsule elastometry, J. Colloid Interface Sci. 513 (2018) 549–565.
[52] J. Lucassen, M. Van Den Tempel, Dynamic measurements of dilational properties of a liquid interface, Chem. Eng. Sci. 27 (6) (1972) 1283–1291.
[53] A. Alicke, L. Stricker, J. Vermant, Model aggregated 2D suspensions in shear and compression: From a fluid layer to an auxetic interface?, J. Colloid Interface Sci. 652 (2023) 317–328.
[54] A. de Groot, J. Yang, L.M.C. Sagis, Surface stress decomposition in large amplitude oscillatory interfacial dilatation of complex interfaces, J. Colloid Interface Sci. 638 (2023) 569–581.
[55] R.A. De Bruijn, Tipstreaming of drops in simple shear flows, Chem. Eng. Sci. 48 (2) (1993) 277–284.
[56] I. Koleva, H. Rehage, Deformation and orientation dynamics of polysiloxane microcapsules in linear shear flow, Soft Matter 8 (13) (2012) 3681–3693.
[57] A. Luciani, M.F. Champagne, L.A. Utracki, Interfacial tension coefficient from the retraction of ellipsoidal drops, J. Polymer Sci. Part B: Polymer Phys. 35 (9) (1997) 1393–1403.
[58] P. Siahcheshm, F. Goharpey, R. Foudazi, Droplet retraction in the presence of nanoparticles with different surface modifications, Rheologica Acta 57 (11) (2018) 729–743.
[59] M.A. Carrozza, M. Hütter, L. Bremer, P.D. Anderson, M.A. Hulsen, Simulation of the extensional deformation of a drop with an elastoviscoplastic interface, J. Non-Newtonian Fluid Mech. 339 (2025) 105408.
[60] N.O. Jaensson, P.D. Anderson, J. Vermant, Computational interfacial rheology, J. Non-Newtonian Fluid Mech. 290 (2021) 104507.